J Mater Sci (2007) 42:3508–3519
DOI 10.1007/s10853-006-0239-9

Contact damage initiation in silicon nitride in Hertzian indentation: role of microstructure

Guang-Yong Lin · Ramaswamy Lakshminarayanan · Dinesh K. Shetty

Received: 29 June 2005 / Accepted: 14 April 2006 / Published online: 20 January 2007

Abstract A bearing-grade silicon nitride with fine microstructure and a turbine-grade silicon nitride with coarse microstructure were studied with respect to the influence of their microstructures on (a) crack-growth-resistance behavior, (b) strength degradation due to Vickers indentation, and (c) crack initiation in quasi-static indentation with WC spheres. The turbine grade exhibited strong rising crack-growth resistance and less strength degradation due to Vickers indentation as compared to the bearing grade. Partial-ring or C cracks initiated in Hertzian indentation and the critical loads exhibited linear (Auerbach) variation with indenter radius above a critical value. For smaller radius, indentation plasticity preceded C-crack initiation. The bearing grade exhibited higher critical loads for C-crack initiation, but showed greater extension toward a ring crack than the turbine grade. These differences in crack initiation and growth were consistent with the differences in crack initiation and propagation toughness of the two grades. A ball-on-ball impact analysis was used to predict the critical velocities for initiating C cracks in the impact of silicon nitride surfaces with WC spheres.

Introduction

Silicon nitride is used in a variety of applications that include cutting tool inserts, automobile engine components such as turbocharger rotors and cam followers and high-performance bearings [1]. These different applications demand different mechanical properties, and, therefore, different microstructures and processing routes for the silicon nitride [2]. In bearing applications, silicon nitride elements may be subjected to contact stresses as high as 4 GPa at ambient and moderate temperatures [3]. Accordingly, silicon nitride bearing elements are processed via sintering and hot-isostatic pressing (HIP) to obtain a fine, uniform microstructure with small β-Si_3N_4 grains and a uniform distribution of a moderate amount of the grain-boundary oxide phase(s). Relatively high strength and hardness and moderate fracture toughness, properties derived from this microstructure, are desirable for bearing applications [4]. High-temperature strength and creep resistance are not as critical for bearing applications, at least at the present time, because there are few applications where silicon nitride elements are used in high-temperature bearings. In turbochargers, silicon nitride rotors are subjected to temperatures around 1030 °C [5] and the service temperatures in gas-turbine engine applications are expected to be even higher [6]. Accordingly, the silicon nitride microstructure and mechanical properties are tailored for high-temperature strength and creep resistance by engineering the grain-boundary oxide phase(s) and their chemical compositions. Typically, the β-Si_3N_4 grains are larger because the components are gas-pressure sintered at a temperature higher than that used in sintering and HIP.

This paper compares the microstructures and the mechanical properties of two commercial grades of silicon nitride. The first, a bearing grade processed by sintering and HIP and designated silicon nitride A in

G.-Y. Lin · R. Lakshminarayanan · D. K. Shetty (✉)
University of Utah, Salt Lake City, UT 84112, USA
e-mail: dinesh.k.shetty@mse.utah.edu

this paper, is widely used in high-performance bearings including the hybrid bearings used in liquid oxygen turbo-pump in the space shuttle's main engine [7]. The second grade, processed by slip casting and gas-pressure sintering and designated silicon nitride B, was developed for gas-turbine engine components [6]. Contact damage and foreign-object damage are of concern in ceramic components, such as bearing elements and rotors in gas-turbine engines. The latter, in particular, can be subjected to impact from carbon particles from the fuel or oxide ceramic particles from the thermal-barrier coatings. The contact-damage resistance of the silicon nitrides was assessed in quasi-static indentation tests and the critical velocities for crack initiation in impact were estimated using an analysis of ball-on-ball impact.

Test materials and procedures

Materials and characterization of microstructures

Billets of fully dense silicon nitrides, 50.8 × 50.8 × 5.0 mm in dimensions, were procured from commercial sources. The microstructures of the silicon nitrides were characterized in a scanning electron microscope using plasma-etched specimen surfaces. As-received materials were first ground with a 320-mesh diamond-grit wheel and followed by grinding with a 600-mesh diamond-grit wheel and polished sequentially with 15, 6 and 1 μm diamond paste. At each stage of grinding or polishing, material was removed to a depth approximately equal to half the thickness of the diamond grit used in the previous stage. This guideline ensured removal of the plastic zones created by the diamond grit and obtained a pristine material surface with minimal residual stress in the final polished state. The polished specimen surfaces were etched using CF_4 dry gas plasma under the following conditions: 0.3 torr pressure, 230 W power, 2 min duration. The etched specimen surfaces were examined in a scanning electron microscope (Cambridge S240) to assess microstructures.

Strength, Young's modulus and fracture toughness measurements

Fracture strengths were measured in four-point bending with beam specimens according to the specifications and procedures described in ASTM Standard C-1161 [8]. Type B specimens (3 × 4 × 45 mm), a support span of 40 mm and a loading span of 20 mm were employed. The tests were conducted on both ground and polished specimens as well as specimens indented with a Vickers diamond pyramid indenter at different loads. A constant crosshead displacement rate of 0.5 mm/min in a displacement-controlled universal testing machine (Model 4206, Instron Corp., Canton, MA) was used. All the tests were conducted in the laboratory ambient (22 °C, 20% relative humidity).

Young's modulus was calculated from the slopes of load-strain plots recorded during the four-point bend tests. The maximum tensile strains in the center span were measured with strain gages mounted on the beam specimens.

Two types of fracture toughness measurements were made in this study. Large crack fracture toughness was measured using chevron-notched, short-bar test specimens [9]. The fracture toughness was calculated from the maximum load, $P_{\max}$, sustained during stable crack growth through the chevron notch:

$$K_{Ic} = \frac{P_{\max}}{B\sqrt{W}} Y_m^* \tag{1}$$

In Eq. (1), B is the specimen thickness, W is the specimen width, and Y_m^* is a non-dimensional stress-intensity coefficient dependent on the specimen and the chevron notch geometry. Munz et al. [10] have calculated values for Y_m^* for different notch geometries. The short-bar specimens used in this study had the following pertinent values: B = 5 mm, W = 20 mm, Y_m^* = 41.84.

Measurements of R-curves

The fracture toughness measurements using chevron-notched test specimens and the pertinent equations used to calculate K_{Ic} are based on the implicit assumption that the fracture toughness of the material is independent of crack length. This assumption is reasonable for fine-grained, polycrystalline ceramics. Coarse-grained ceramics and ceramics self-reinforced with elongated grains, for example, silicon nitrides with elongated β-Si_3N_4 grains, exhibit rising crack-growth resistance with crack length or R-curves. The R-curves for the two silicon nitrides employed in this study were assessed by measuring the equilibrium lengths of cracks produced on indentation with a Vickers diamond pyramid indenter and their stable extension under a far-field stress. Ramachandran and Shetty [11] have described the details of the pertinent experiments and the theoretical analyses. The experiments employed multiple indents on each specimen, a method developed by Cook and Lawn [12] to capture the crack lengths at fracture. The procedure consisted

of indenting ground and polished surfaces of four-point-bend specimens with a Vickers diamond pyramid indenter at three locations, at the center of the 4 × 45 mm surface and at 5 mm on either side. All the three indents on a specimen were made at the same load. Figure 1(a) shows a Vickers indent and the surface traces of the half-penny cracks aligned with the diagonals of the Vickers impression produced at 150 N load on silicon nitride A. Crack-growth resistance was calculated from the initial radius, c_0, of the half-penny cracks and the indentation load, P, using the following equation [13, 14]:

$$K_R(c_0) = \delta\left(\frac{E}{H}\right)^{1/2}\frac{P}{c_0^{3/2}} \tag{2}$$

In Eq. (2), δ is a non-dimensional constant that depends only on the indenter geometry and the Poisson's ratio of the material, E is the elastic modulus and H is the hardness of the material. Measurements of the equilibrium crack radius, c_0, as a function of the indentation load, P, gave one set of measurements of K_R as a function of crack radius, c_0, using the pertinent values of E, H and δ. Values of $\delta = 0.0226$ and $\delta = 0.0255$ were calculated for silicon nitrides A and B using a procedure described by Krause [15] and briefly outlined in a later section.

Following the measurements of c_0 the indented specimens were loaded in four-point bending to fracture. Under a far-field applied stress, the half penny cracks extended stably to a surface length, c^*, at the fracture stress, σ_f. Fracture resistance corresponding to crack length c^* was calculated using the following equation [16, 17]:

$$K_R(c^*) = \delta\left(\frac{E}{H}\right)^{1/2}\frac{P}{c^{*3/2}} + 2\Omega\sigma\left(\frac{c^*}{\pi}\right)^{1/2} \tag{3}$$

In Eq. (3), Ω is a stress-intensity coefficient that accounts for free surface correction and stress-gradient effects. Unstable crack extension occurred at the fracture stress, σ_f, and the instability crack length, c^*. Fracture occurred from one of the three equivalent indents leaving the other two to give a measure of the instability crack length, c^*. Figure 1(b) shows the stably extended half penny crack corresponding to the initial crack shown in Fig. 1(a). Measurements of fracture stress, σ_f, crack length at instability, c^*, and Eq. (3) gave a second set of measurements of K_R. The measurements based on both c_0 and c^* were combined to define the R-curves over an extended range of crack lengths for the two silicon nitrides. Values of Ω were estimated from the numerical calculations of Newman and Raju [18].

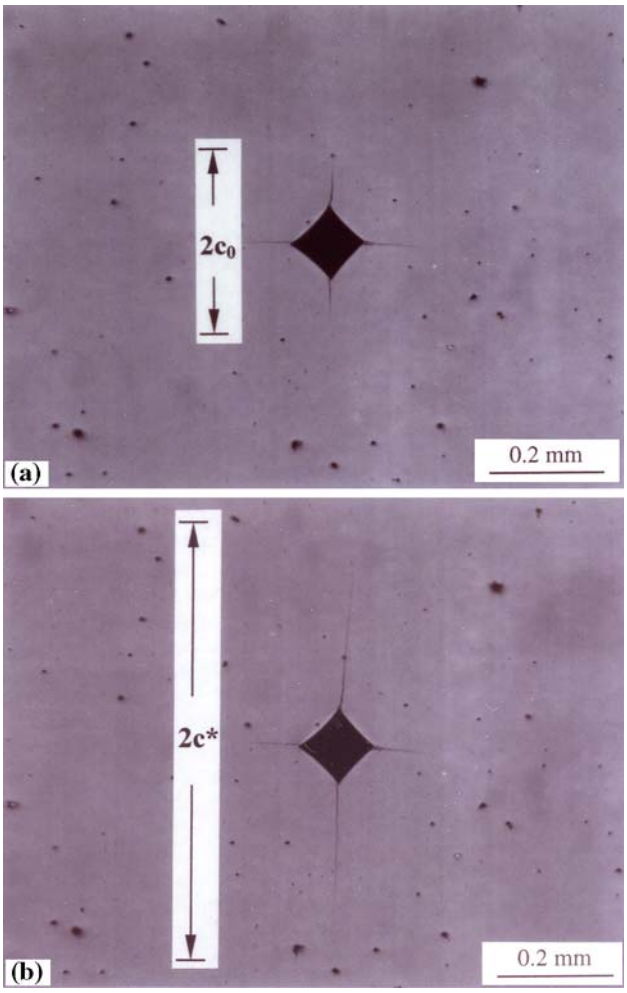

Fig. 1 Representative Vickers indentation cracks in silicon nitride A: (**a**) as-indented cracks at P = 150 N, (**b**) indentation cracks after stable extension

Measurements of crack-initiation loads in Hertzian indentation

The critical loads for initiating partial-ring cracks in Hertzian indentation were measured using the following procedure. The polished surfaces of the silicon nitrides were indented with WC–Co balls at various loads. At each load, ten indentations were made and the cumulative probability of cracking at that load was defined as the fraction of ten that produced cracks. The load range was selected to vary the probability of cracking from 0 to 1. Figure 2 shows an example of the cumulative probability of cracking plots for Hertzian indentation of silicon nitrides A and B using WC–Co balls 2 mm in radius. The probability of cracking was zero up to a threshold load, P_0, increased linearly from

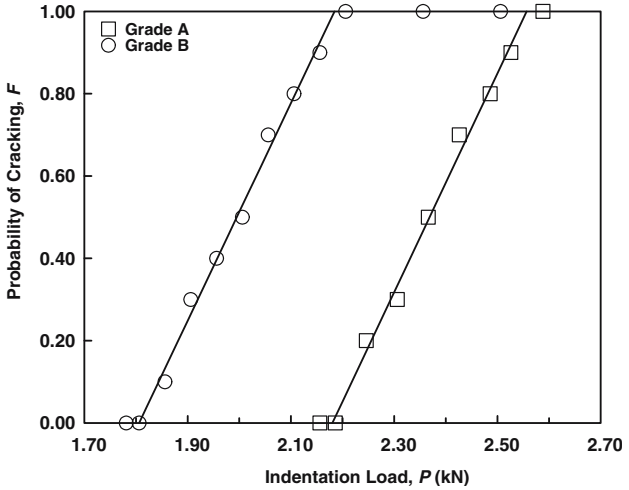

Fig. 2 Plots of cumulative probability of crack initiation (F) versus indentation load (P) for silicon nitrides A and B in Hertzian indentation with 2 mm radius WC–Co balls

the threshold to an upper-bound load, P_u, and was constant at 1 for $P > P_u$. An average crack-initiation load, $\bar{P}_c$, was defined from the following equation with P_0 and P_u calculated from linear fits to the cumulative probability plots as shown by the solid lines in Fig. 2:

$$\bar{P}_c = \int_0^1 P(F)\mathrm{d}F = \left(\frac{P_0 + P_u}{2}\right) \tag{4}$$

In Eq. (4), F is the cumulative probability of cracking at an indentation load P defined by the following equation:

$$F(P) = \left(\frac{P - P_0}{P_u - P_0}\right) \tag{5}$$

The standard deviation of the critical load for cracking was defined by the following equation:

$$s = \left[\int_0^1 \left(P - \bar{P}_c\right)^2 \mathrm{d}F\right]^{1/2} = \frac{(P_u - P_0)}{2\sqrt{3}} \tag{6}$$

The linear fits to the probability plots were typically based on six or seven values of $F(P)$ in the range, $0 < F < 1$. Experiments were repeated for WC–Co balls varying in radius from 0.4 to 2.0 mm.

Results and analysis

Microstructures and properties of silicon nitrides

Figure 3(a, b) shows the microstructures of silicon nitrides A and B, respectively. In each microstructure,

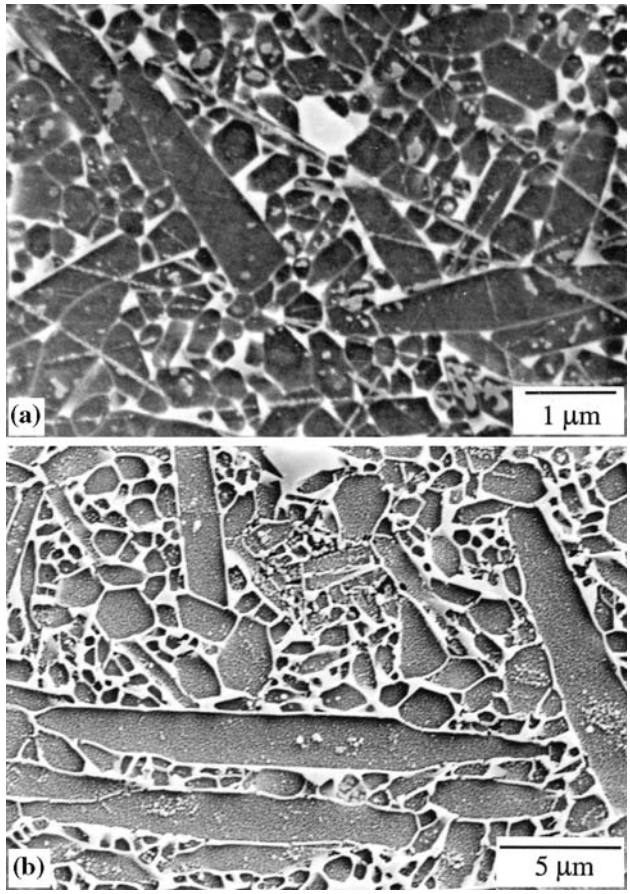

Fig. 3 Microstructures of silicon nitrides: (**a**) bearing-grade and (**b**) gas-turbine grade

the darker phase is β-Si_3N_4 grains, while the lighter phase consists of oxides derived from the sintering additives. The average length and aspect ratio of the β-Si_3N_4 grains and their standard deviations are listed in Table 1. The numbers listed in parentheses in Table 1 are the numbers of independent measurements of the particular property. Both the average grain length and the average aspect ratio of the β-Si_3N_4 grains were greater for the turbine grade than for the bearing grade.

Table 1 also lists Young's modulus and the mechanical properties of the silicon nitrides measured in this study. The values of the Poisson's ratio and density were obtained from the product literature supplied by the material vendors. The bearing-grade silicon nitride exhibited higher strength and hardness because of its fine microstructure, while the turbine grade had higher fracture toughness, roughly twice that of the bearing grade. These results are consistent with the reported influence of microstructure of silicon nitrides on mechanical properties [2].

Table 1 Microstructural parameters and properties of silicon nitrides A and B

Property	Silicon Nitride A	Silicon Nitride B
β-Si_3N_4 Grains		
Length (μm)	2.0 ± 0.4 (180)	8.9 ± 4.1 (120)
Aspect ratio	3.3 ± 1.2 (180)	4.6 ± 2.6 (120)
Young's modulus, E (GPa)	308 ± 5 (3)	300 ± 5 (3)
Poisson's ratio, ν	0.29	0.26
Vickers hardness[a], H (GPa)	15.60 ± 0.11 (6)	14.95 ± 0.21 (6)
Fracture toughness[b], K_{Ic} (MPa $\sqrt{}$ m)	5.15 ± 0.06 (5)	10.06 ± 1.06 (5)
Density, ρ (g/cm^3)	3.23	3.41
Fracture strength, σ_f (MPa)	912 ± 40.5 (5)	725 ± 35 (5)
R-curve parameters		
K_0 (MPa $\sqrt{}$ m)	6.2	5.0
K_∞ (MPa $\sqrt{}$ m)	7.6	10.7
λ (μm)	115.6	171.2
A (MPa $\sqrt{}$ m·m^{-n})	14.17	23.96
n	0.082	0.118
$\bar{\Omega}$	1.0685	1.0620

[a] Measured at 300 N load

[b] Measured by the short-bar test method

Crack-growth-resistance (R-curves) of silicon nitrides

Crack-growth-resistance or R-curves for the two silicon nitrides assessed from Vickers indentation crack lengths, c_0 after indentation (filled symbols) and c^* at instability under far-field applied load (open symbols), are shown in Fig. 4. There was a distinct trend of increasing crack-growth resistance with increasing crack length, especially for the turbine-grade silicon nitride with the coarse microstructure. The solid lines fitted to the experimental data are the 'best fits' of the following empirical equation suggested by Ramachandran and Shetty [11]:

$$K_R(c) = K_\infty - (K_\infty - K_0)\exp\left(-\frac{c}{\lambda}\right) \quad (7)$$

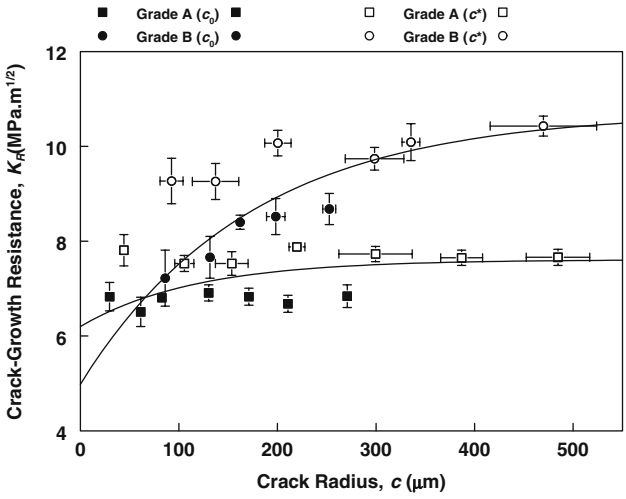

Fig. 4 Crack-growth-resistance (R-curves) curves of silicon nitrides assessed from Vickers indentation cracks

In Eq. (7), K_0 and K_∞ are empirical parameters that represent the crack-initiation toughness and the plateau toughness, respectively, and λ is a crack length normalizing parameter. Note that $K_R(c) = K_0$ for $c = 0$ and K_R (c) $\rightarrow$ K_∞ for $c >> \lambda$. The values of the three empirical parameters, K_∞, K_0 and λ, obtained by fitting Eq. (7) to the data of Fig. 4 by minimizing the total variance by iterative regression, are listed in Table 1. The plateau toughness, K_∞, for silicon nitride B was close to the fracture toughness measured in the short-bar tests. For silicon nitride A, however, both the crack-initiation toughness and the plateau toughness of the R-curve were greater than the fracture toughness measured in the short-bar tests. The strong R-curve behavior noted for silicon nitride B in this study is similar to those reported by Li and Yamanis [19] and Ramachandran and Shetty [11] for silicon nitrides with similar microstructures. These silicon nitrides are commonly referred to as self-reinforced because of the reinforcing effect of a small fraction of large β-Si_3N_4 grains in a matrix of smaller β-Si_3N_4 grains.

Fracture strengths and strength degradation

Fracture strengths of the silicon nitrides, measured in the initial ground and polished condition and after Vickers indentation at different loads, are plotted in Fig. 5 as log σ_f versus log P plots. The initial strengths are plotted in Fig. 5 on the y-axis corresponding to P = 1 N for convenience. Both materials exhibited degradation of strength as a result of Vickers indentation. However, silicon nitride B, the turbine grade with the coarse microstructure and the strong R-curve behavior, exhibited less degradation in strength as compared to the bearing grade A. Thus, for example, the fracture

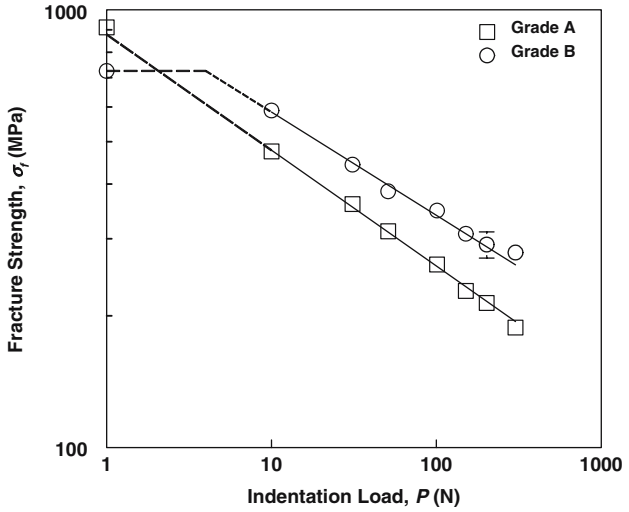

Fig. 5 Fracture strengths of silicon nitrides before and after indentation with a Vickers indenter at different loads

strength of grade A decreased from 912 MPa to 188 MPa when indented with a Vickers indenter at a load of 300 N. For the same indentation load, fracture strength of grade B decreased from 725 MPa to 279 MPa.

Fracture strength of ceramics indented with a Vickers diamond pyramid indenter has been modeled for both cases of flat (crack-length independent) crack-growth resistance [17] and rising crack-growth resistance (R-curve) [15, 20]. For the case of flat crack-growth resistance, the fracture strength is given by the following equation [17]:

$$\sigma_f = \frac{3\pi^{1/2}K_c}{8\bar{\Omega}}\left[\frac{K_c}{4\chi P}\right]^{1/3} \tag{8}$$

In Eq. (8), K_c is the fracture toughness and χ is a non-dimensional parameter defined by the following equation:

$$\chi = \delta\left(\frac{E}{H}\right)^{1/2} \tag{9}$$

Based on Eq. (8), one expects a plot of log σ_f versus log P to be linear with a slope of –0.33. As seen in Fig. 5, the plots of log σ_f versus log P are quite linear for both grades A and B. However, the slopes of the best linear fits (solid lines in Fig. 5) are –0.264 and –0.236 for grades A and B, respectively. Such deviations have been attributed to rising crack-growth resistance or R-curve behavior. Cook and Clarke [21] and Krause [15] employed an empirical power-law equation to describe R-curve behavior:

$$K_R(c) = Ac^n \tag{10}$$

Eq. (10) leads to the following equation for the strength of a ceramic after Vickers indentation at a load P [15]:

$$\sigma_f = \frac{(3+2n)\pi^{1/2}A}{8\bar{\Omega}}\left[\frac{(1-2n)A}{4\chi P}\right]^{\frac{(1-2n)}{(2n+3)}} \tag{11}$$

Note that Eq. (11) predicts strength degradation only for $n < 0.5$ and in the limit, $n \rightarrow 0$, Eq. (11) reduces to Eq. (8). The empirical parameters A and n extracted from the linear plots of log σ_f versus log P of Fig. 5 using Eq. (11) are also listed in Table 1. The values of χ and, therefore, δ, were calculated from the slopes of plots of $c_0^{(3+2n)/2}$ versus P, as described by Krause [15].

Evaluation of either the fracture toughness, K_c, from Eq. (8) or the R-curve parameters, A and n, from Eq. (11) using indentation strength data such as those shown in Fig. 5 has some limitations. First, it was noted in section "Measurements of R-curves" that Ω is a coefficient that accounts for free-surface and stress-gradient effects on stress intensity. Ω also depends on the aspect ratio of the half-ellipse surface crack (c/a, where a is the depth of the crack) and the aspect ratio increases with increasing crack size. The combined effect is a decrease in Ω with increase in crack size [18]. The derivations of Eqs. (8) and (11) assume that Ω is constant and independent of crack size. Therefore, an average value, $\bar{\Omega}$, pertinent to the range of instability crack lengths, c^*, measured in the strength tests is used in Eq. (8) or Eq. (11) (see Table 1). This is one source of error in the value of K_c or A and n calculated from strength data. Secondly, the power-law function, Eq. (10), is physically unappealing because the crack-growth resistance can range from zero to infinity with increasing crack length. Because of these limitations the power-law function assessed from strength data give poor fits to the R-curve data from crack-length measurements in Fig. 4.

The exponential function, Eq. (7), is more compatible with physically-based models of toughening that typically invoke a threshold matrix toughness (K_0), an increment in toughness due to a bridging zone that saturates for large crack lengths ($= K_\infty - K_0$), and the length scaling parameter, λ, related to the saturation bridging zone length. The function, however, is not amenable to obtaining a closed-form relation between strength and indentation load. Numerical solutions obtained by Ramachandran and Shetty [20] do indicate, however, that log σ_f versus log P plots for Eq. (7) are just as linear as for the power-law relation.

Linearity of the log σ_f versus log P plots is not a good indicator of the functional form of the governing R-curve.

Crack initiation in Hertzian loading

The variations of the average crack-initiation load with the radius of the WC–Co balls are plotted in Fig. 6 for silicon nitride grades A and B. Note that in the log $\bar{P}_c$ - log R plots of Fig. 6 the error bars do not appear because they are too small relative to the size of the symbols. For both materials, the average crack-initiation load increased linearly with the ball radius for ball radii, $R \geq 1.0$ mm:

$$\bar{P}_c = \alpha R \tag{12}$$

The crack-initiation loads were consistently lower for silicon nitride B relative to silicon nitride A. The linear variation of the crack-initiation load with ball radius is referred to as Auerbach's law [22]. Roesler [23] recognized that Eq. (12) represents an energy-balance criterion based on the following Hertzian equation for the total elastic strain energy stored in the ball and the plate, U, normalized by the contact area, πa^2:

$$\frac{U}{\pi a^2} = \frac{2}{5\pi}\frac{P}{R} \tag{13}$$

Using Eq. (13) Roesler [23] rationalized Auerbach's law as corresponding to an energy balance criterion whereby a fixed fraction of the total elastic energy stored is dissipated in the form of a crack whose area scales with the contact area. The respective fractions were thought to be independent of the ball radius.

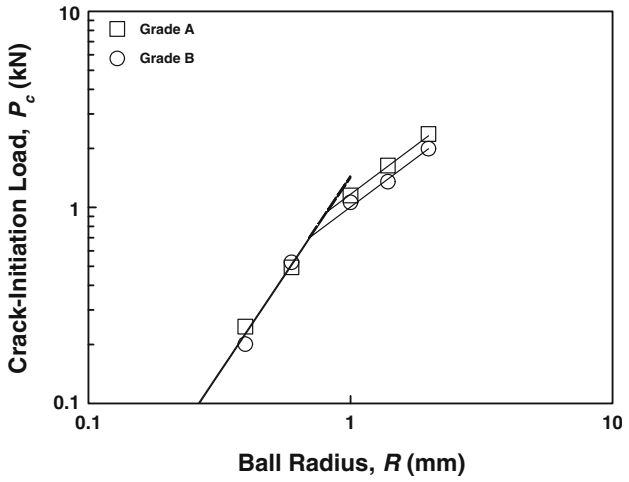

Fig. 6 Variations of the average crack-initiation loads, $\bar{P}_c$, with WC–Co ball radius for silicon nitrides A and B

A number of investigators have developed analytical expressions for the constant α in the Auerbach's relation. Roesler's energy-balance argument, for example, leads to the following equation for α [23]:

$$\alpha = \frac{5\pi}{2}\frac{\theta}{\eta}\gamma \tag{14}$$

In Eq. (14), θ is the crack-surface area normalized by the contact area, η is the fraction of the elastic energy released during crack initiation, and γ is the fracture-surface energy per unit area. Numerical values for θ and η are not easy to calculate, however, because both depend on the shape and the size of the C crack at nucleation.

The indented surfaces of the specimens were examined to assess the shape and size of the C cracks. Figure 7(a, b) shows optical photographs of C cracks formed on indentation with 2 mm radius WC–Co balls

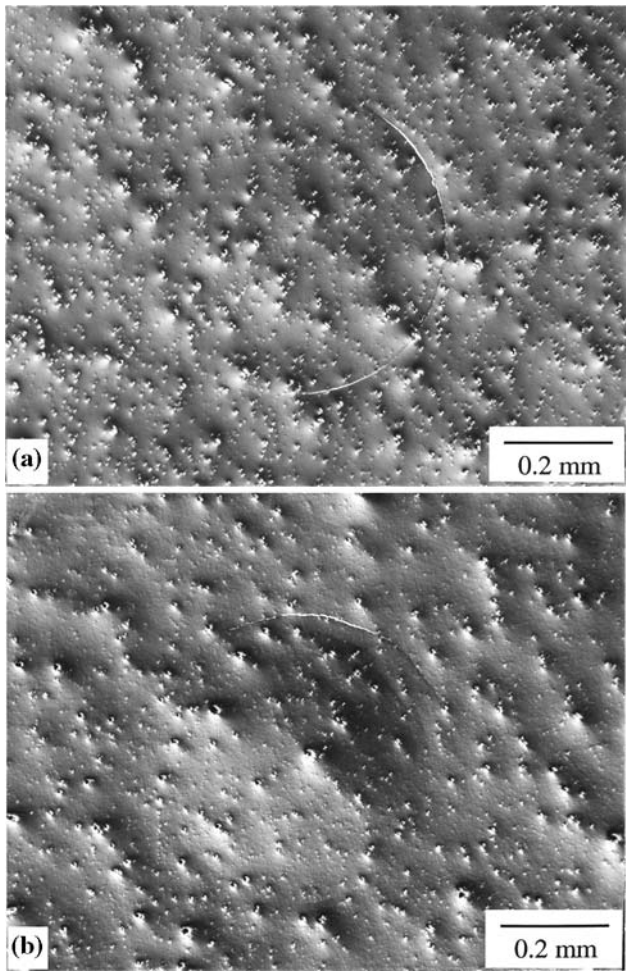

Fig. 7 Partial ring cracks formed on indentation with 2 mm radius WC–Co balls: (**a**) silicon nitride A, $P =$ 2.4 kN, (**b**) silicon nitride B, $P =$ 2.0 kN

on silicon nitride A at $P = 2.4$ kN and on silicon nitride B at $P = 2.0$ kN, respectively. Note that these loads correspond to approximately 50 % probability of cracking in the respective materials. Under these conditions, silicon nitride A showed a C crack that enveloped approximately 50 % of the contact circle, while in silicon nitride B the crack spanned only about 25 % of the contact circle. The lower crack-initiation load of silicon nitride B is likely due to its lower crack-initiation toughness (K_0), while the shorter length of the C crack is likely due to its higher crack-growth resistance (ΔK_∞). For both materials, the arc length of the C crack increased from a threshold value to the full ring crack as the indentation load increased from P_0 to P_u. Thus, the probability distribution curves of Fig. 2 reflect both unstable crack initiation and arrest close to the threshold load and some stable growth with increasing load. Plots of P_0 and P_u versus R showed trends similar to $\bar{P}_c$ with slopes bracketing those shown in Fig. 6. Thus, Auerbach's law is applicable to short C cracks formed at initiation as well as full ring cracks resulting from stable growth of the C cracks. It is not clear to what depths the C cracks and the ring cracks penetrate below the surface at these loads. The depth of penetration must be proportional to the diameter of the contact circle for Roesler's energy-balance argument to be valid.

The critical loads for C crack initiation with balls, $R < 1$ mm, showed a deviation from the linear Auerbach relation. As seen in Fig. 6, the critical loads for crack initiation in this regime are below the linear extrapolations and show greater dependence on R. The log $\bar{P}_c$ versus log R plots indicated that for small ball radii the C-crack-initiation load could be described by the following equation:

$$\bar{P}_c = \beta R^2 \tag{15}$$

The lines fitted through the data points at $R = 0.4$ mm and $R = 0.6$ mm in Fig. 6 are the 'best fits' of Eq. (15). To understand the origin of this deviation at small ball radii, the indented surfaces were examined in an optical microscope. Figure 8 shows an example of an indent made at $P = 0.304$ kN with a WC–Co ball of 0.4 mm radius on silicon nitride B. A plastic impression of the spherical indenter is clearly evident on the surface. A nearly complete ring crack can be noted along the crater edge. If plastic indentation occurs when the maximum contact stress under the indenter reaches the value of the hardness, H, it can be readily shown that the plastic indentation load, P_I, must scale with R^2 according to the following equation [24]:

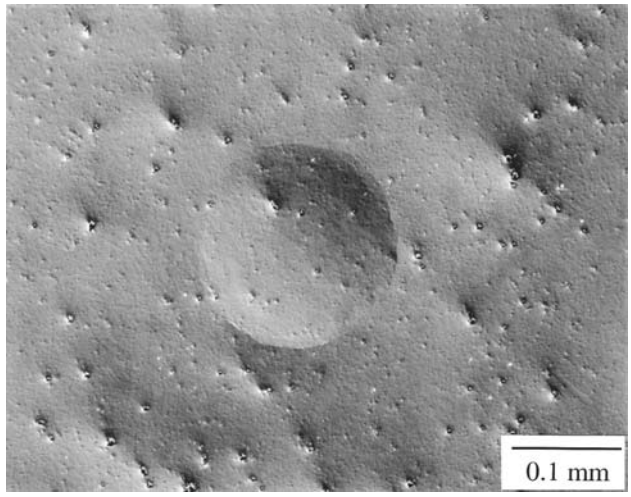

Fig. 8 Plastic impression and ring crack along the crater edge on silicon nitride B indented with a 0.4 mm radius WC–Co ball at 0.304 kN load

$$P_I = \frac{1}{6}\left[\frac{(1-\nu_1^2)}{E_1} + \frac{(1-\nu_2^2)}{E_2}\right]^2 H^3 R^2 \tag{16}$$

In Eq. (16), E and ν are Young's modulus and Poisson's ratio, respectively, and the subscripts 1 and 2 correspond to the indenter and the substrate, respectively. The similar dependences on R of $\bar{P}_c$ and P_I suggests that for small indenter radii the critical load for crack initiation is likely governed by a critical value of the plastic strain in indentation.

Discussion

Recent studies of the effects of size and shape of the self-reinforcing β-Si_3N_4 grains and of the sintering additives have improved our current understanding of the role of the microstructure in the enhanced fracture toughness of self-reinforced silicon nitrides [25, 26]. A distinct bimodal size distribution for β-Si_3N_4 grains achieved by seeding [25] and control of the chemistry of the inter-granular amorphous phase, specifically a high Y:Al ratio and low nitrogen content in the Si-Al-O-N glasses [26], are key factors in achieving a high steady-state (plateau) fracture toughness while maintaining a high fracture strength for self-reinforced silicon nitrides. The contribution of the crack-bridging β-Si_3N_4 grains to the fracture toughness of self-reinforced silicon nitrides can be modeled using the same general approach as that used for whisker-reinforced ceramics [27]. For small-scale bridging, the steady-state (plateau) fracture toughness of the

composite, K_c, can be expressed in terms of the matrix (fine-grained silicon nitride) toughness, K_m, and the contribution of the ligaments [28, 29]:

$$\frac{K_c}{K_m} = \left[1 + \frac{E\Delta G_c}{(1-\nu^2)K_m^2}\right]^{1/2} \tag{17}$$

In Eq. (17), ΔG_c is the contribution of the ligaments to the energy-release rate defined in terms of an appropriate stress (σ)-displacement (u) relation [28, 29]:

$$\Delta G_c = f \int_0^{u_c} \sigma(u)\mathrm{d}u \tag{18}$$

In Eq. (18), f is the area fraction of the bridging β-Si_3N_4 grains and u_c is the critical crack-opening displacement at the end of the bridging zone where the closure traction goes to zero. The functional form of $\sigma(u)$ depends on the nature of the bridging ligament (elastic, elastic-plastic, etc) and the mechanisms of energy dissipation in the bridging zone. Becher et al. [27] have pointed out that multiple mechanisms may contribute to ΔG_c simultaneously. For elastic β-Si_3N_4 grains that debond, stretch and frictionally slide until fracture, the model developed by Becher et al. [30] for whisker reinforcement can be modified and applied to self-reinforced silicon nitride

$$\Delta G_c = \frac{(\sigma_f^r)^2 f d \gamma_m}{36 E \gamma_i} \tag{19}$$

In Eq. (19), σ_f^r is the fracture strength of the bridging β-Si_3N_4 grains, d is the diameter of the bridging grains, and γ_m and γ_I are the matrix and the interface toughness, respectively. An attempt was made to see if the R-curve parameters measured in this study for the two silicon nitrides, specifically the ratio, (K_∞/K_0), can be compared with the model prediction, Eq. (17). It is recognized that this comparison is tenuous at best because values of the material and microstructure parameters, such as σ_f^r, f, γ_m and γ_I are unavailable. Further, the model is strictly applicable to silicon nitrides with distinct bimodal size distributions for β-Si_3N_4 grains and the two grades used in this study did not exhibit such a duplex grain structure. It was, therefore, assumed that all of the parameters that appear in Eq. (19), except for the diameter of the reinforcing β-Si_3N_4 grains, were the same for grades A and B. Next, using the ratio, $(K_\infty/K_0) = (7.6/6.2) = 1.226$ for grade A, a value for the normalized toughness increment from the bridging zone, $[E\Delta G_c/(1-\nu^2)K_m^2] = 0.503$, was calculated for grade A. For grade B, this term must be (1.935/0.606) larger because of the larger bridging grain size. This leads to a toughening ratio, $(K_c/K_m) = 1.614$. The measured toughening in grade B is $(K_\infty/K_0) = (10.7/5.0) = 2.14$. This suggests that the R-curve and the toughening increment measured in grade B relative to grade A cannot be entirely due to its larger β-Si_3N_4 grain size. There must be a second contribution to the toughness increase in grade B and one possibility is an increased value for f, the area fraction of the bridging grains in grade B relative to grade A.

Contact damage in brittle materials under loading with spherical indenters has been studied for well over 100 years. Lawn [22] has reviewed this work beginning with the classical theoretical and experimental studies of Hertz [31] and Auerbach [32]. Most of the early work, up until the 1960s, was on inorganic glasses with spherical steel indenters. A major focus of this early research was on measuring critical loads for crack initiation and interpreting the dependence of the critical loads on the indenter radius. As noted in section ''Crack initiation in Hertzian loading'', a linear dependence of $\bar{P}_c$ on R, was first rationalized by Roesler [23] in terms of an energy-balance criterion. Central to this argument is the idea that area of the initiated crack scales with the contact area, while the same fraction of the stored elastic energy is released independent of the ball radius. The Auerbach constant, α, is not easy to calculate, however, because both θ and η depend on the crack shape and size, and there is no clear understanding of the shape and size of the cracks at initiation. Frank and Lawn [33] examined the stability of a cone crack in the decreasing stress field under a spherical indenter by calculating stress-intensity factors by Green's function method. The stress-intensity factor for a cone crack was expressed in the following form [34]:

$$K\left(\frac{c}{a}\right) = p_0 a^{1/2} I\left(\frac{c}{a}, \psi, \nu\right) \tag{20}$$

In Eq. (20), p_0 is the average pressure on the contact area and I is a dimensionless integral that accounts for the variation of the principal maximum (tensile) stress along the trajectory of the cone crack (length, c) and the radius of the ring crack relative to the contact circle, ψ. Calculations of I as a function of c/a showed a range of crack lengths where cone cracks grow stably to a length c^* at a critical load P_c, become unstable at c^*, arrest at a longer cone crack size, and continue stable growth. By using the fracture criterion, $K = K_c$, the fracture toughness of the material, and expressing p_0 and a in terms of the applied load and the indenter

radius, they derived the following form of Auerbach's law:

$$\bar{P}_c = \frac{4\pi^2 k}{3I^{*2}} \frac{K_c^2}{E} R \tag{21}$$

In Eq. (21), k is a dimensionless parameter dependent on the elastic properties of the indenter and the substrate, E is Young's modulus of the substrate, and I^* is the value of I for $c = c^*$. The derivation of the Auerbach's law in the form of Eq. (21) is based on two precepts: (a) the crack-initiation event corresponds to instability and arrest of a cone crack after an initial period of stable growth, and (b) the decreasing stress field along the trajectory of the cone crack is responsible for the initial stability followed by instability and arrest of the cone crack.

An interesting question to address is whether Eq. (21) is applicable to crack initiation in the silicon nitrides studied here. As shown in Fig. 7(a, b), the cracks that form at the average measured values of $\bar{P}_c$ are C cracks or partial-ring cracks. It is unlikely that cone cracks form below the surface before the ring cracks form completely on the surface because of the steep drop in tensile stress below the surface. The bright arcs seen in Fig. 7(a, b) are most likely surface traces of shallow surface cracks. The stability of these cracks during their growth around the contact circle in the load range P_0 to P_u must be due to the R-curves of the materials. The observed fact that the average critical load, $\bar{P}_c$, increases linearly with R (see Fig. 6) suggests that Roesler's energy-scaling argument is still valid for these shallow C cracks. It is unlikely that Eq. (21) developed for cone cracks would be applicable to these three-dimensional surface cracks.

The transition from $\bar{P}_c \propto R^2$ to $\bar{P}_c \propto R$ with increasing R seen in Fig. 6 can be viewed as a ductile-brittle transition at a critical indenter radius, R_c. For $R < R_c$, plastic indentation precedes C-crack initiation, while for $R > R_c$, C-crack initiation occurs before plastic indentation. Such ductile-brittle transitions have been observed for many materials [24]. Lee et al. [35] observed such transitions in two hot-pressed silicon nitrides with medium and coarse microstructures obtained by hot pressing at different temperatures. Since significant amount of plasticity develops under the indenter before any cracks appear for $R < R_c$, the stress field must be modified significantly from the elastic (Hertzian) stress field. As a result, Auerbach's law, typically observed in the dominant elastic regime ($R > R_c$) is not likely to hold for $R < R_c$. The fact that $\bar{P}_c \propto R^2$ for $R < R_c$ suggests that C-crack initiation in this regime occurs at a critical plastic strain, (a/R).

As noted in the introduction, contact damage and foreign-object-impact damage are of concern in silicon nitride bearings and gas-turbine-engine components. Large silicon nitride balls are susceptible to form C cracks as a result of impacts during ball finishing and subsequent handling [36]. Turbo-charger rotors and gas-turbine engine components suffer impact damage by solid particles derived from the fuel or thermal-barrier coatings [37, 38]. An attempt was made to see if the critical velocities for initiating cracks in ball-on-plate impact could be predicted using the $\bar{P}_c$ versus R data obtained in the quasi-static experiments (Fig. 6). For this purpose, we consider the general problem of the impact of a sphere of radius, R_1, and elastic properties, E_1, ν_1, on a second sphere of radius, R_2, and elastic properties, E_2, ν_2 as indicated in the schematic of Fig. 9. A simple analysis of this problem (see Timoshenko and Goodier [39]) results in the following equation for the maximum force generated in the impact at an initial velocity, v:

$$P_{\max} = \left[\frac{16}{9\pi^2} \frac{R_1 R_2}{(k_1 + k_2)^2 (R_1 + R_2)}\right]^{1/5} \left[\frac{5v^2 m_1 m_2}{4(m_1 + m_2)}\right]^{3/5} \tag{22}$$

In Eq. (22), m_1 and m_2 are the masses of the spheres, and k_1 and k_2 are defined by the following equations:

$$k_1 = \frac{(1 - \nu_1^2)}{\pi E_1}, \quad k_2 = \frac{(1 - \nu_2^2)}{\pi E_2} \tag{23}$$

Shockey et al. [40] measured critical velocities for initiating ring cracks on hot-pressed silicon nitride plates in impact tests with WC balls (E_1 = 630 GPa, ν_1 = 0.26, ρ_1 = 15.0 g/cc). The critical velocity for ring-crack initiation, v_c, was estimated from the following equation derived from Eq. (22) using the conditions, $R_2 \to \infty$, $m_2 \to \infty$, and $P_{\max} = \bar{P}_c$:

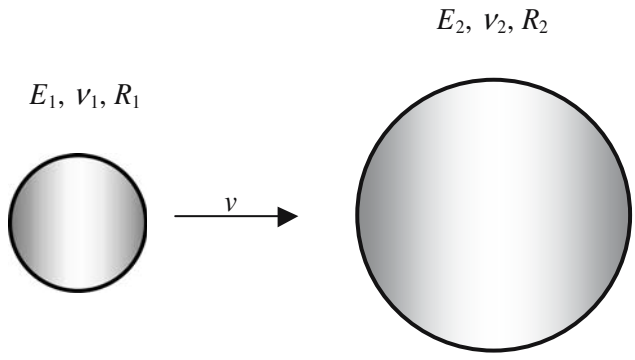

Fig. 9 A schematic of a sphere of radius, R_1, and elastic properties, E_1 and ν_1, impacting a second sphere of radius, R_2, and elastic properties, E_2 and ν_2

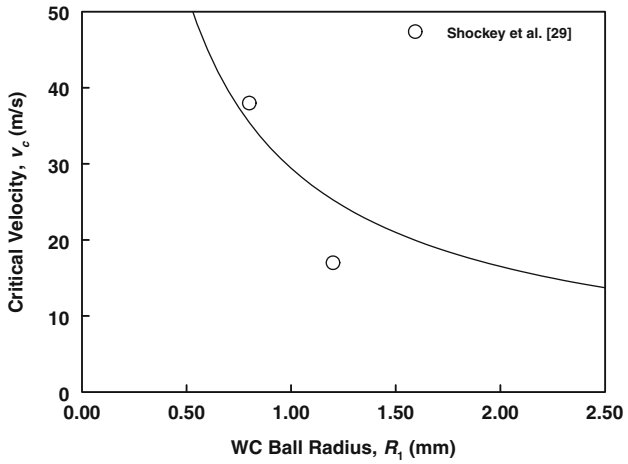

Fig. 10 Variation of the critical velocity for initiating cracks with WC spheres impacting a flat silicon nitride surface

$$v_c = \left[\frac{3E_1}{5\pi\rho_1(1-\nu_1^2)}\right]^{1/2}\left[\frac{9\left(1+\frac{k_2}{k_1}\right)^2}{16}\right]^{1/6}\left[\frac{\bar{P}_c(1-\nu_1^2)}{E_1R_1^2}\right]^{5/6} \quad (24)$$

Figure 10 compares a plot of v_c versus R_1 predicted using Eq. (24) with the measurements of Shockey et al. [40]. The solid curve is based on the linear Auerbach relation for silicon nitride A in Fig. 6 and the elastic properties of silicon nitride A and WC. The agreement is reasonable in view of the fact that the silicon nitride used by Shockey et al. [40] was a different grade of material than grade A of this study.

Conclusions

1. The turbine-grade silicon nitride with the coarse microstructure exhibited strong rising crack-growth-resistance behavior and less strength degradation due to Vickers indentation as compared to the bearing grade with the fine microstructure.
2. A simple analysis of the R-curves using a model of toughening from a zone of crack-bridging β-Si_3N_4 grains indicated that the higher fracture toughness of grade B was likely due to both an increased diameter as well as an increased fraction of the bridging grains.
3. The critical loads for initiating C cracks in indentation with spherical indenters followed the linear Auerbach relation for radii greater than a critical value. Indentation plasticity preceded C-crack initiation for smaller radii.
4. C cracks initiated at lower loads in the turbine grade silicon nitride because of its lower crack-initiation toughness. The extension of the C cracks was, however, limited by the rising crack-growth resistance.
5. The critical velocities of impact with WC spheres for initiating C cracks on silicon nitride surfaces could be predicted with reasonable accuracy using a kinematic relation and the critical loads measured in quasi-static indentation.

Acknowledgements Research at University of Utah was supported by a subcontract under the DARPA-AMP Cooperative Agreement No. N00014-96-2-0014 with Sunstrand Aerospace Company.

References

1. Jack KH (2000) Mater Sci Forum 325–326:255
2. Tajima Y (1993) In: Silicon nitride ceramics, scientific and technological advances, Materials Research Society Symposium 287:189
3. Wang L, Snidle RW, Gu L (2000) Wear 246:159
4. Cundill RT (1992) In: Carlsson R, Johannson T, Kahlman L (eds) 4th International Symposium on Ceramic Materials and Components for Engines, Goteborg, Sweden, 1991, Elsevier Science Publishers, Ltd, p 905
5. Kawase H, Kato K, Matsuhisa T, Mizuno T (1993) Trans ASME J Eng Gas Turbines Power 115:23
6. Yoshida M, Truruzono S, Ono T, Gejima H (1994) Proc Int Gas Turbine Aeroengine Cong Expo, Paper # 94-GT-332
7. Boggs RN (1995) Design News, January 23
8. ASTM Standard C-1161-90 (1990) Standard test method for flexural strength of advanced ceramics at ambient temperature, American Society for Testing and Materials, Philadelphia, PA
9. Munz D, Bubsey RT, Shannon JL Jr (1980) J Test Eval 8:103
10. Munz D, Bubsey RT, Srawley JE (1980) Int J Fracture 16:359
11. Ramachandran N, Shetty DK (1991) J Am Ceram Soc 74:2634
12. Cook RF, Lawn BR (1983) J Am Ceram Soc 66(11):C-200
13. Marshall DB, Lawn BR (1979) J Mater Sci 14:2001
14. Lawn BR, Evans AG, Marshall DB (1980) J Am Ceram Soc 63(9–10):574
15. Krause RF Jr (1988) J Am Ceram Soc 71(5):338
16. Marshall DB, Lawn BR, Chantikul P (1979) J Mater Sci 14:2225
17. Chantikul P, Anstis GR, Lawn BR, Marshall DB (1981) J Am Ceram Soc 64(9):539
18. Newman Jr JC, Raju IS (1981) Eng Frac Mech 15:291
19. Li CW, Yamanis J (1989) Ceram Eng Sci Proc 10:632
20. Ramachandran N, Shetty DK (1993) J Mater Sci 28:6120
21. Cook RF, Clarke DR (1988) Acta Metall 36(3):555
22. Lawn BR (1998) J Am Ceram Soc 81:1977
23. Roesler FC (1956) Proc Phys Soc London B69:55
24. Evans AG, Wilshaw TR (1976) Acta Metall 24:939
25. Becher PF, Sun EY, Plucknett KP, Alexander KB, Hsueh CH, Lin HT, Waters SB, Westmoreland CG, Kang ES, Hirao K, Brito ME (1998) J Am Ceram Soc 81(11):2821

26. Sun EY, Becher PF, Plucknett KP, Hsueh CH, Alexander KB, Waters SB, Hirao K, Brito ME (1998) J Am Ceram Soc 81(11):2831
27. Becher PF, Hwang SL, Lin HT, Tiegs TN (1994) In: Hoffmann MJ, Petzow G (eds) Tailoring of mechanical properties of Si_3N_4 ceramics. Kluwer Academic Publishers, Boston, pp 87–100
28. Evans AG, McMeeking RM (1986) Acta Metall 34(12):2435
29. Budiansky B, Amazigo JC, Evans AG (1988) J Mech Phys Solids 36(2):167
30. Becher PF, Hsueh CH, Angelini P, Tiegs TN (1988) J Am Ceram Soc 71(12):1050
31. Hertz H (1896) Hertz's Miscellaneous Papers; Chapters 5 and 6. Macmillan, London, UK
32. Auerbach F (1891) Ann Phys Chem 43:61
33. Frank FC, Lawn BR (1967) Proc R Soc London A299:291
34. Lawn BR (1993) Fracture of brittle solids, chap. 8. Cambridge University Press, p 283
35. Lee SK, Wuttiphan S, Lawn BR (1997) J Am Ceram Soc 80:2367
36. Cundill RT (1997) In: Niihara K (ed) 6th International Symposium on Ceramic Materials and Components for Engines. Arita, Japan
37. Akimune Y, Akiba T, Ogasawara T (1995) J Mater Sci 30:1000
38. Yoshida H, Nakashima T, Yoshida M, Hara Y, Shimamori T (1998) Proc Int Gas Turbine and Aeroengine Cong Expo, Paper # 98-GT-399
39. Timoshenko SP, Goodier JN (1970) Theory of elasticity, 3rd edn. p 420
40. Shockey DA, Rowcliffe DJ, Dao KC, Seaman L (1990) J Am Ceram Soc 73:1613